

Amphiphilic block polymer-based self-assembly of high payload nanoparticles for efficient combinatorial chemo-photodynamic therapy

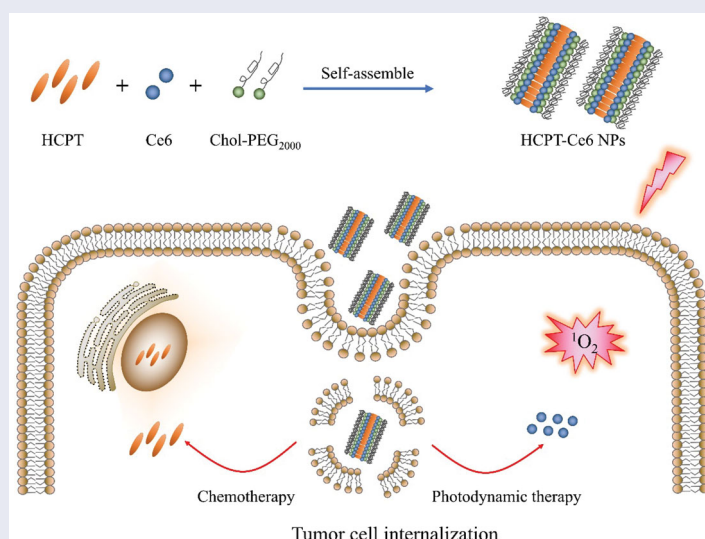
Qisan Ma^a, Yanna Zhao^a, Qingran Guan^a, Yuping Zhao^a, Huaizhen Zhang^b, Zhuang Ding^a, Qingpeng Wang^a, Yushu Wu^a, Min Liu^{a,c} and Jun Han^a

^aInstitute of Biopharmaceutical Research, Liaocheng University, Liaocheng, Shandong, PR China; ^bSchool of Environment and Planning, Liaocheng University, Liaocheng, Shandong, PR China; ^cSchool of Chemistry and Chemical Engineering, Liaocheng University, Liaocheng, Shandong, PR China

ABSTRACT

Combinatorial chemo-photodynamic therapy is regarded as effective cancer therapy strategy, which could be realized via multiple nano-drug delivery system. Herein, novel high payload nanoparticles stabilized by amphiphilic block polymer cholesterol-*b*-poly(ethylene glycol) (PEG)₂₀₀₀ (Chol-PEG₂₀₀₀) were fabricated for loading chemotherapeutic drug 10-hydroxycamptothecin (HCPT) and photosensitizer chlorin e6 (Ce6). The obtained HCPT/Ce6 NPs showed uniform rod-like morphology with a hydration diameter of 178.9 ± 4.0 nm and excellent stability in aqueous solution. HCPT and Ce6 in the NPs displayed differential release profile, which was benefit for preferentially exerting the photodynamic effect and subsequently enhancing the sensitivity of the cells to HCPT. Under laser irradiation, the NPs demonstrated fantastic *in vitro* and *in vivo* anticancer efficiency due to combinatorial chemo-photodynamic therapy, enhanced cellular uptake effectiveness, and superb intracellular ROS productivity. Besides, the NPs were proved as absent of systemic toxicity. In summary, this nanoparticle delivery system could be hopefully utilized as effective cancer therapy strategy for synergistically exerting combined chemo-photodynamic therapy in clinic.

GRAPHICAL ABSTRACT



ARTICLE HISTORY

Received 5 October 2020
Revised 4 November 2020
Accepted 9 November 2020

KEYWORDS

Amphiphilic block polymer; 10-hydroxycamptothecin; chlorin e6; high payload nanoparticles; combinatorial chemo-photodynamic therapy

1. Introduction

Nowadays, cancer is still known as the major threaten to human health and clinically utilized chemotherapy occupies the main status in cancer treatment (Wang et al., 2017).

Conventional chemotherapy represents the routine administration of chemotherapeutic drugs via intravenous injection or oral medication. Although more and more novel chemotherapeutic agents have been discovered or synthesized

CONTACT Yanna Zhao  ynzhao2011@163.com; Jun Han  junhanmail@163.com Institute of Biopharmaceutical Research, Liaocheng University, Liaocheng, Shandong, PR China

 Supplemental data for this article can be accessed [here](#).

© 2020 The Author(s). Published by Informa UK Limited, trading as Taylor & Francis Group.

This is an Open Access article distributed under the terms of the Creative Commons Attribution-NonCommercial License (<http://creativecommons.org/licenses/by-nc/4.0/>), which permits unrestricted non-commercial use, distribution, and reproduction in any medium, provided the original work is properly cited.

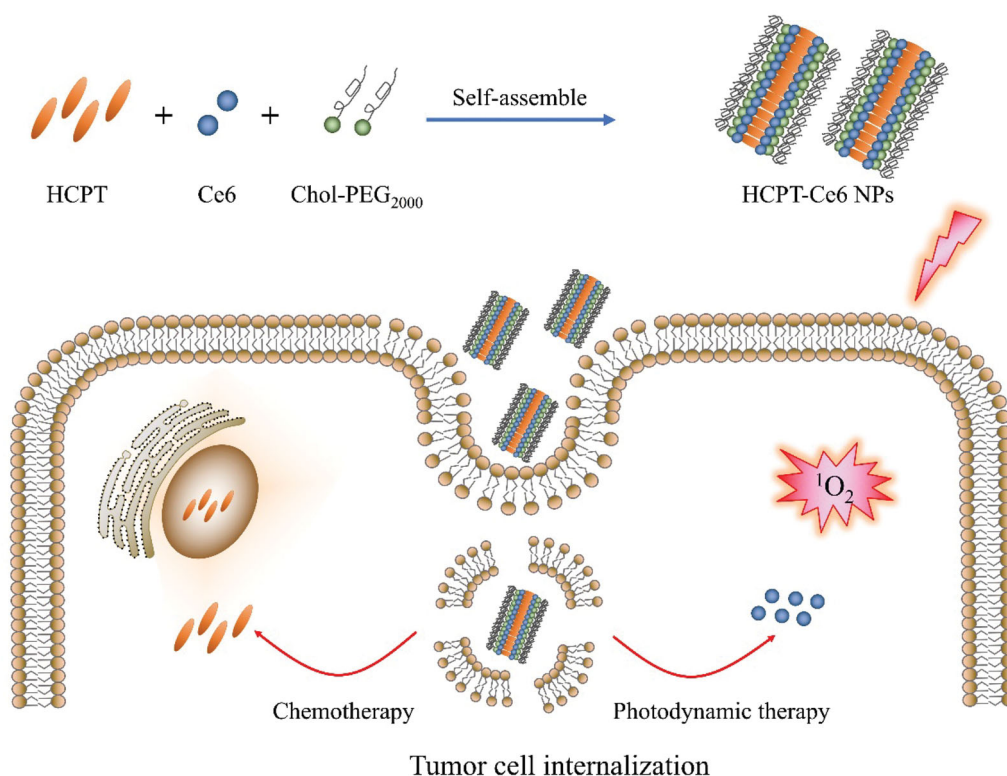
during the past century, the efficiency of the agents is still limited by their poor bioavailability and systemic toxicity due to non-targeted distribution (Qi et al., 2017). Besides, multi-drug resistance (MDR) in cancer cells also triggers failure of chemotherapy (Hu et al., 2017). In contrast to chemotherapy, photodynamic therapy (PDT), a marginally invasive therapeutic modality, only takes effect in specific area where photosensitizers (PSs) produce spatiotemporally controlled cytotoxic reactive oxygen species (ROS), which results in negligible systemic toxicity (Zheng et al., 2020). However, attributed to poor solubility, rapid pharmacokinetics, and unsatisfactory photostability of the PSs, the application of PDT is merely restricted to preclinical practices in most circumstances (Kim et al., 2020).

In consideration of the boundedness of monotherapy strategy, combinatorial chemo-photodynamic therapy has been developed for improving their therapeutic outcome and diminishing their side effect in recent years (Li et al., 2020). Thus, nano-drug delivery system (NDDS), which could integrate two or more agents into one delivery system, has been fabricated for combining chemotherapy and photodynamic therapy (Yan et al., 2018). NDDS could enhance the therapeutic effect in comparison to free drugs because of the so-called enhanced permeability and retention (EPR) effect, which contributes to their accumulation in tumor (Sun et al., 2019). NDDS is also expected to conquer MDR in tumors as it could accomplish increased circulation time, stylized drug release behavior and improved cellular uptake (Niazi et al., 2016; Bar-Zeev et al., 2017). Notably, as the ROS produced by the pre-released PSs could oxygenize the membrane of the NDDS-encapsulated endosome in cancer cells and accelerate the release of the simultaneously loaded

chemotherapeutic agents [photochemical internalization (PCI) phenomenon], NDDS could promisingly achieve synergistic effect of combinatorial chemo-photodynamic therapy (Nishiyama et al., 2005; Gao & Lo, 2018).

Under some circumstances, the fabrication of NDDS relies on amphiphilic block polymers carrying poly(ethylene glycol) (PEG) as hydrophilic segment in view of their excellent biocompatibility and biodegradability (Li & Niu, 2018). The driving force for the assembly of amphiphilic block polymers should be ascribed to the solubility difference between hydrophilic segments and hydrophobic blocks, which spontaneously self-aggregate into typically core-shell structure eventually in aqueous environment and benefit for drug encapsulation (Feitosa et al., 2019). Besides, the PEG corona around the NDDS plays an important role in decreasing the possibility of phagocytosis and metabolism by reticuloendothelial system (RES), which increases its blood circulation time (Li et al., 2011). Although numerous block copolymers approved by FDA are accessible for applying in drug delivery, the inferior drug loading content (typically no more than 20%) of the NDDS raises the production cost (Zhou et al., 2013).

In this work, high payload 10-hydroxycamptothecin/chlorin e6 NPs (HCPT/Ce6 NPs) (Scheme 1) were fabricated with amphiphilic block polymer cholesterol-*b*-poly(ethylene glycol) (PEG)₂₀₀₀ (Chol-PEG₂₀₀₀) as stabilizer via facile antisolvent precipitation approach to achieve combinational chemo-photodynamic effect. Physicochemical characteristics including size, zeta potential and morphology of the NPs were investigated, while the intracellular ROS [especially singlet oxygen (¹O₂)] production efficiency was thoroughly analyzed. Furthermore, the *in vitro* and *in vivo* antitumor



Scheme 1. Illustration of HCPT/Ce6 NPs and the NPs guided chemo-PDT combinational therapy.

efficacy of the combinatorial chemo-photodynamic therapy were assessed particularly.

2. Experimental section

2.1. Materials

Chlorin e6 (Ce6) and 10-hydroxycamptothecin (HCPT) were purchased from Dalian Meilun Biotechnology Co., Ltd (Dalian, China). Cholesterol-*b*-poly(ethylene glycol) (PEG)₂₀₀₀ (Chol-PEG₂₀₀₀) was obtained from Xi'an ruixi Biological Technology Co., Ltd (Xi'an, China). Singlet oxygen sensor green reagent (SOSG) and 2',7'-Dichlorodihydrofluorescein diacetate (DCFH-DA) were supplied by Dalian Meilun Biotechnology Co., Ltd (Dalian, China). 3-(4,5-Dimethylthiazol-2-yl)-2,5-diphenyl tetrazolium bromide (MTT) was purchased from Sigma Aldrich Chemicals (Germany). RPMI-1640 was supplied by Hyclone Thermo Scientific (Waltham, MA, USA). Penicillin and streptomycin were procured from Gibco Thermo Scientific (Waltham, MA, USA). Fetal bovine serum (FBS) was obtained from Excell Bio (Shanghai, China). All the other chemical reagents were of commercially accessible analytical grade and used directly throughout the experiments without further purification.

2.2. Animals and cell lines

Female BALB/c mice (6–8 weeks, 20 ± 2 g) were purchased from Jinan Pengyue experimental animal breeding co. LTD (Jinan, China). All the animal experimental procedures were strictly performed abide by the guidelines and protocols for Animal Experiments Ethical and Regulatory approved by the Animal Ethics Committee of Liaocheng University.

4T1 (murine mammary carcinoma) cell lines were obtained from the Cell Culture Center, Institute of Basic Medical Sciences (Beijing, China) and cultured at 37 °C with 5% CO₂ atmosphere in RPMI-1640 medium supplemented with 10% fetal bovine serum, and 100 units/mL of penicillin G and streptomycin.

2.3. Preparation of HCPT/Ce6 NPs

The high payload 10-hydroxycamptothecin (HCPT)/chlorin e6 (Ce6) nanoparticles (HCPT/Ce6 NPs) were fabricated via commonly used antisolvent precipitation method (Guo et al., 2017b). Briefly, certain amount of HCPT, Ce6 and Chol-PEG₂₀₀₀ (at a ratio of 3:1:4, mol/mol) were co-dissolved in 1 mL of *N,N*-dimethylformamide (DMF), which was immediately added dropwise to 15 mL deionized water at room temperature under ultrasonication (40 KHz, 480 W). After that, the ultrasonication was continued for 10 min, and then the mixture was dialysis against deionized water (1L × 4 times) to eliminate residual DMF. High-pressure homogenization was conducted for 15 min to decrease the particle size of the obtained HCPT/Ce6 NPs with a D-3L homogenizer (PhD, Fort Wayne, IN, USA) at around 100 MPa. Moreover, single-drug NPs with Chol-PEG₂₀₀₀ as stabilizer including 10-hydroxycamptothecin nanoparticles (HCPT NPs) and chlorin e6 NPs

(Ce6 NPs) were also prepared via the same method for comparison.

2.4. Characteristics of HCPT/Ce6 NPs

Particle size, polydispersity index (PDI) and zeta potential (ZP) of HCPT/Ce6 NPs were analyzed by dynamic light scattering (DLS, Zetasizer Nano ZSP, Malvern, UK). Morphology of HCPT/Ce6 NPs was detected with both scanning electron microscopy (SEM, S-4800, Hitachi Limited., Japan) and transmission electron microscope (TEM, JEM-2100, JEOL, Japan). For SEM analysis, the samples were sputter-coated with conductive gold-palladium (Au/Pd) layer. For TEM detection, the samples were stained with uranyl acetate (2%, w/v). Infrared (IR) spectra in the region 500–4000 cm⁻¹ were obtained from FT-IR spectrometer (Nicolet 6700, Thermo Scientific, Waltham, MA, USA) via KBr pellet method.

2.5. In vitro release assay

The *in vitro* release profiles of HCPT/Ce6 NPs were investigated via traditional dialysis method (Guo et al., 2017a). Briefly, 2 mL of diluted HCPT/Ce6 NPs was put in a dialysis bag (MWCO, 8–14 kDa), which was then immersed in 100 mL of PBS (0.1 M, pH 7.4) involving 1% (w/v) SDS. The experiment was conducted for about 120 h, during which 3.0 mL of the release medium was withdrawn at set time intervals and replaced by fresh release medium of equal volume. The detection for HCPT was carried out with high performance liquid chromatography (HPLC) after sample filtration by 0.22 μm syringe-driven filter (Millipore, Billerica, MA, USA). The wavelength for UV detector was set at 409 nm, while a C18 column (4.6 mm × 250 mm, 5 μm, Agilent) was utilized for analysis. The mobile phase composed of acetonitrile and 0.1% acetic acid (28/72, v/v) and applied at a flow rate of 1 mL/min. Besides, the detection for Ce6 was conducted with an F-4600 fluorescence spectrophotometer (Hitachi, Japan) at an excitation (E_x) wavelength of 503 nm and an emission (E_m) wavelength of 660 nm. The slits for both E_x and E_m were 10 nm. The *in vitro* release assay was repeated for three times.

2.6. Intracellular singlet oxygen (¹O₂) detection

2',7'-Dichloro-dihydro-fluorescein diacetate (DCFH-DA), a fluorescent probe typically utilized for detecting the intracellular singlet oxygen (¹O₂) amount, was applied in this study. DCFH-DA could easily permeate the cell membrane and immediately hydrolyze into the non-fluorescent product 2',7'-dichloro-dihydro-fluorescein (DCFH) in the presence of cellular esterases. Then DCFH will be oxidized to 2',7'-dichloro-fluorescein (DCF), which could emit bright green fluorescence (Liu et al., 2015). Briefly, 1 × 10⁴ cells were placed in a 24-well plate and cultured for 12 h with serum-contained basal medium. Then the medium was replaced by serum-free medium containing different formulations and the incubation continued for another 6 h. PBS was utilized to wash the cells and serum-free medium involving DCFH-DA (10 μM) was

added. After incubation for 30 min, the cells were washed with PBS and irradiated with laser (660 nm, 5 mW) for different time intervals. An IX-71 inverted fluorescence microscope (Olympus, Japan) was applied for the observation of DCF fluorescent.

2.7. In vitro cytotoxicity assay

The *in vitro* cytotoxicity of HCPT/Ce6 NPs against 4T1 cells was performed via classical MTT assay. Briefly, 4T1 cells were seeded in 96-well plates (8×10^3 cells/well) and incubated for 12 h with serum-contained complete medium. Then the culture medium was substituted by serum-free medium involving various formulations. Cells treated with HCPT/Ce6 NPs (with laser) and Ce6 NPs (with laser) were irradiated for 10 min with laser (660 nm, 5 mW) after incubating for 4 h. The incubation continued for totally 48 h, ended with adding 20 μ L of MTT solution (5 mg/mL) to each well. MTT reagent was discarded after another 4 h, and 150 μ L of DMSO was appended. A microplate reader (BioTek, Winooski, VT, USA) was applied for analyzing the absorbance of each well at a wavelength of 490 nm. Cell viability (%) was calculated via the following equation: Cell viability (%) = $(A_{\text{treated}}/A_{\text{control}}) \times 100\%$. A_{treated} was the absorbance of the groups treated with different formulations, while A_{control} was the absorbance of the group treated with blank serum-free culture medium. Graphpad Prism of version 5.0 (Graphpad, San Diego, CA, USA) was used to figure out half maximal inhibitory concentration (IC_{50}) values, while CompuSyn software of version 1.0 (ComboSyn, Paramus, NJ, USA) was utilized to calculate combination index (CI_x) values. All the experiments were completed in quintuplicates.

2.8. In vitro cellular uptake assay

The *in vitro* cellular uptake assay of HCPT/Ce6 NPs were performed via both HPLC and fluorescence microscope. Briefly, 4T1 cells (2×10^4 cells/well) were plated in a 24-well plate and incubated overnight in complete medium. Then the medium was replaced by serum-free medium containing different formulations. At set time intervals, the medium was discarded and the cells were washed with PBS in triplicate.

For HPLC analysis (the analysis of HCPT), the cells were treated with various formulations at different HCPT concentrations, which were collected and disintegrated by RIPA lysis buffer after incubation. Acetonitrile was added for protein deproteinization, while the supernatant obtained by centrifugation was utilized for HPLC analysis. HPLC method of HCPT was the same as mentioned above except that the UV detector was replaced by a fluorescence detector (excitation wavelength = 409 nm, emission wavelength = 535 nm). The established calibration curves possessed a correlation coefficient of more than 0.99. Moreover, several cellular uptake inhibitors such as sucrose, methyl- β -cyclodextrin (M β CD), and cytochalasin B (CCB) were employed for the investigation of the cellular uptake mechanism of HCPT/Ce6 NPs.

For the internalization observation of HCPT/Ce6 NPs (the fluorescence observation of Ce6), the cells were treated with

HCPT/Ce6 NPs at a Ce6 concentration of 5 μ g/mL, which were fixated by paraformaldehyde and stained with LysoTracker Green DND-26 (Sigma, St. Louis, MO, USA) and Hoechst 33258 (Life Technologies, Carlsbad, CA, USA), respectively, after incubation. Furthermore, PBS was applied to wash off the excess reagent and the fluorescence observations were conducted with an IX-71 inverted fluorescence microscope (Olympus, Japan).

2.9. In vivo antitumor efficacy assay

The *in vivo* antitumor efficacy assay was performed on 4T1-tumor bearing mice models. Briefly, 5×10^6 4T1 cells were subcutaneously inoculated into the right armpit of female BALB/c mice, which were grouped randomly into 5 groups ($n=6$). When the volume of the tumor reached 50–80 mm³ (implantation for around 4 days), the administration started. The control group received saline, while the test groups received HCPT NPs, Ce6 NPs (with laser) and HCPT/Ce6 NPs (with or without laser) at a HCPT-equivalent dosage of 6 mg/kg and a Ce6-equivalent dosage of 3 mg/kg, respectively. The administration was conducted once every two days for 10 days via intravenous injection. The mice treated with Ce6 NPs (with laser) and HCPT/Ce6 NPs (with laser) were irradiated with laser (660 nm, 5 mW) for around 20 min at the tumor site after administration for 4 h. The tumor volume of each mouse was monitored every day throughout the 10 days, which was calculated via the following equation: V (mm³) = $0.5 \times L \times S^2$, where L is on behalf of the larger diameter and S represents the smaller diameter of the tumor. The body weight of the mice was also measured every day as an index of toxicity. Moreover, at 10th day, the mice were sacrificed and their main organs, together with the tumor tissues were removed, washed with saline and studied by histological analysis via hematoxylin and eosin (H&E) staining method. Alanine aminotransferase (ALT), aspartate aminotransferase (AST), and blood urea nitrogen (BUN), which were index for hepatic and renal function, were analyzed to further disclose the biosafety of the test groups.

2.10. Statistical analysis

Data were processed as mean \pm standard deviation (SD) for all experiments. Statistical analysis was performed via independent-samples *t*-test and one-way analysis of variance (ANOVA) (SPSS 19.0, IBM, Armonk, NY, USA). *p* Value less than .05 ($p < .05$) was deemed as statistically significant, and *p* value less than .001 ($p < .001$) was considered as highly significant.

3. Results and discussion

3.1. Characterization of high payload HCPT/Ce6 NPs

3.1.1. Particle size and morphology

As shown in Figure 1(A,B), high payload HCPT/Ce6 NPs (DLC of HCPT: 31.87%; DLC of Ce6: 13.21%, Supplementary Table S2) prepared via antisolvent precipitation method with

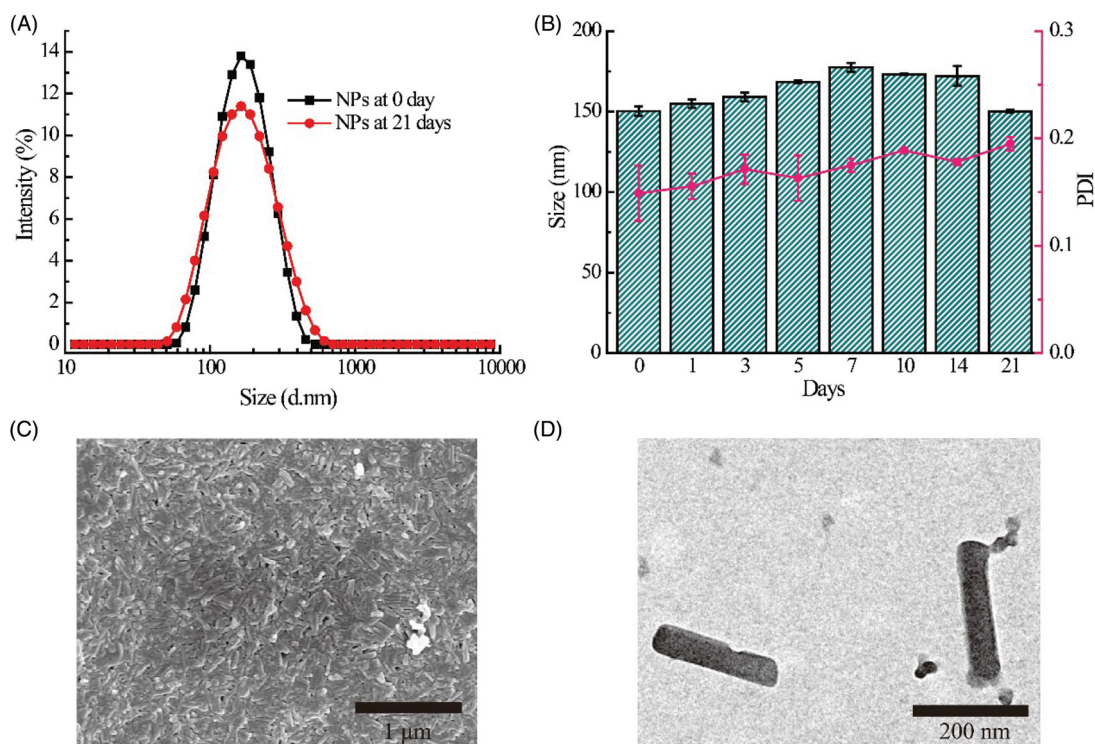


Figure 1. The particle size distribution of HCPT/Ce6 NPs before vs. after storage determined by DLS results (A) and the particle size changes of HCPT/Ce6 NPs during storage ($n = 3$) (B); SEM images of HCPT/Ce6 NPs (C); TEM images of HCPT/Ce6 NPs (D).

stabilizer Chol-PEG₂₀₀₀ showed hydrodynamic particle size of 178.9 ± 4.0 nm, narrow size distribution with a PDI of 0.176 ± 0.004 , and excellent storage stability due to high zeta potential value of -22.4 ± 0.8 mV (in the range of 20~30 mV) (Su et al., 2020). Besides, the morphology of HCPT/Ce6 NPs exhibited uniform nanorods in shape without signs of agglomeration via both SEM and TEM (Figure 1(C,D)). As shown in the photographs, the authentic size of the nanorods was around 200 nm in length and 50 nm in width (in the range of 50~300 nm), which could be beneficial to extend their blood circulation time, enhance their cellular uptake and increase their tumor accumulation (Liu et al., 2017). Moreover, it was reported that NPs possessing negative surface charge would exhibit preferential accumulation at tumor site rather than at regular organs site (Xiao et al., 2011), which might also help lengthening the circulation time of the NPs because of effectively avoiding renal drug clearance (Sun et al., 2017). The particle size of the NPs observed by SEM and TEM was totally different from that measured by DLS, which was attributed to the distinction between the two analytical method: for DLS, the hydration diameter was obtained from the equivalent sphere of the NPs, while SEM or TEM acquired the actual image of the dry NPs (Chen et al., 2019a).

3.1.2. Ultraviolet-visual (UV-Vis) and fluorescence spectroscopy

Spectroscopy is an efficient method to disclose the structural and conformational changes of molecules (Zhao et al., 2020). As shown in Figure 2(A), the absorbance spectra of HCPT/Ce6 NPs exhibited broader and slightly quenched bands at

the wavelength of 268 nm, 338 nm and 380 nm for HCPT and 405 nm for Ce6 in comparison with HCPT NPs and Ce6 NPs, which were measured at the same HCPT/Ce6 concentration. Besides, the absorbance band of HCPT/Ce6 NPs at the wavelength of 380 nm showed significantly red-shifted compared to HCPT NPs. All the results verified that hydrophobic interactions possibly existed among the drugs and the stabilizer Chol-PEG₂₀₀₀, and HCPT/Ce6 NPs were not merely the mixture of the two single drug NPs (Liu et al., 2016). Moreover, the fluorescence spectra (Figure 2(B)) of HCPT/Ce6 NPs at the wavelength of 540 nm for HCPT and 650 nm for Ce6 in contrast to HCPT NPs and Ce6 NPs at the same HCPT/Ce6 concentration also exhibited significantly quenched profiles, which verified the excitonic migration among the molecules. That was to say, non-covalent association such as hydrophobic interactions might occur among the ternary system (Zhang et al., 2016).

3.1.3. FT-IR spectroscopy

Figure 2(C) showed the FT-IR spectra of raw HCPT, raw Ce6, raw Chol-PEG₂₀₀₀, physical mixture of HCPT/Ce6/Chol-PEG₂₀₀₀, and HCPT/Ce6 NPs. The characteristic peaks at 1723, 1654, 1595 and 1503 cm^{-1} in the spectrum of raw HCPT were assigned to the C=O stretching vibration, acylamino group, aromatic frame, and aromatic ring, respectively (Jing et al., 2020), while the spectrum bands of raw Ce6 focused on 2923 and 2853 cm^{-1} (asymmetric and symmetric C-H stretching vibrations), 1715 cm^{-1} (carbonyl stretching C=O vibration), 1601 cm^{-1} (C=C stretching vibration), together with 1510 cm^{-1} and 1448 cm^{-1} (aromatic frame) (Wu et al., 2019). Besides, the intensive and broad peak at 2890 and 1113 cm^{-1} in the spectrum of raw Chol-PEG₂₀₀₀ mainly

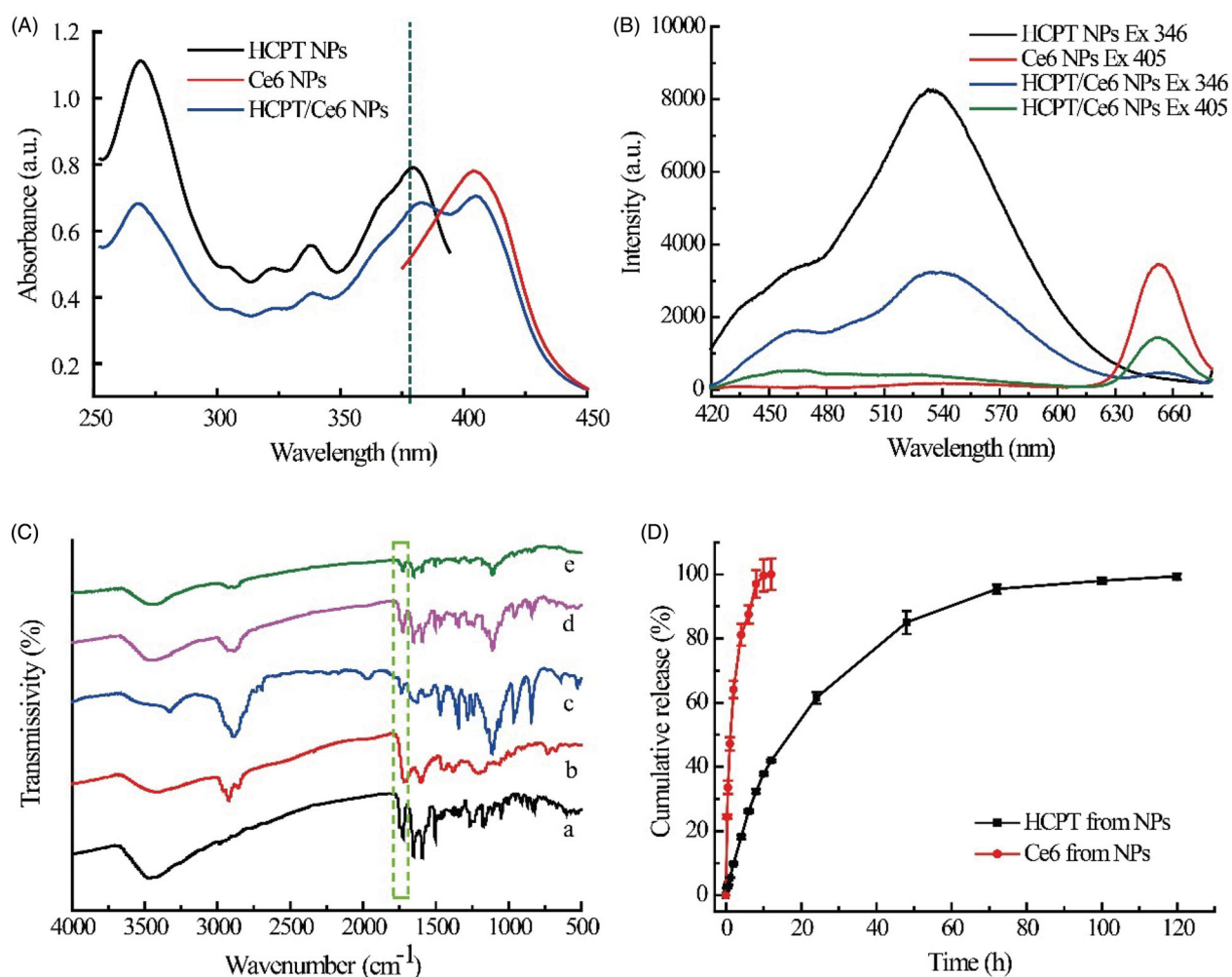


Figure 2. The UV-vis absorption spectra (A) and fluorescence spectra (B) of HCPT NPs, Ce6 NPs and HCPT/Ce6 NPs; FT-IR spectra (C) of (a) raw HCPT, (b) raw Ce6, (c) raw Chol-PEG₂₀₀₀, (d) physical mixture of HCPT, Ce6 and Chol-PEG₂₀₀₀, and (e) HCPT/Ce6 NPs; Cumulative release profiles of HCPT and Ce6 from HCPT/Ce6 NPs in 0.1 M PBS (pH 7.4) involving 1% (w/v) SDS ($n = 3$) (D).

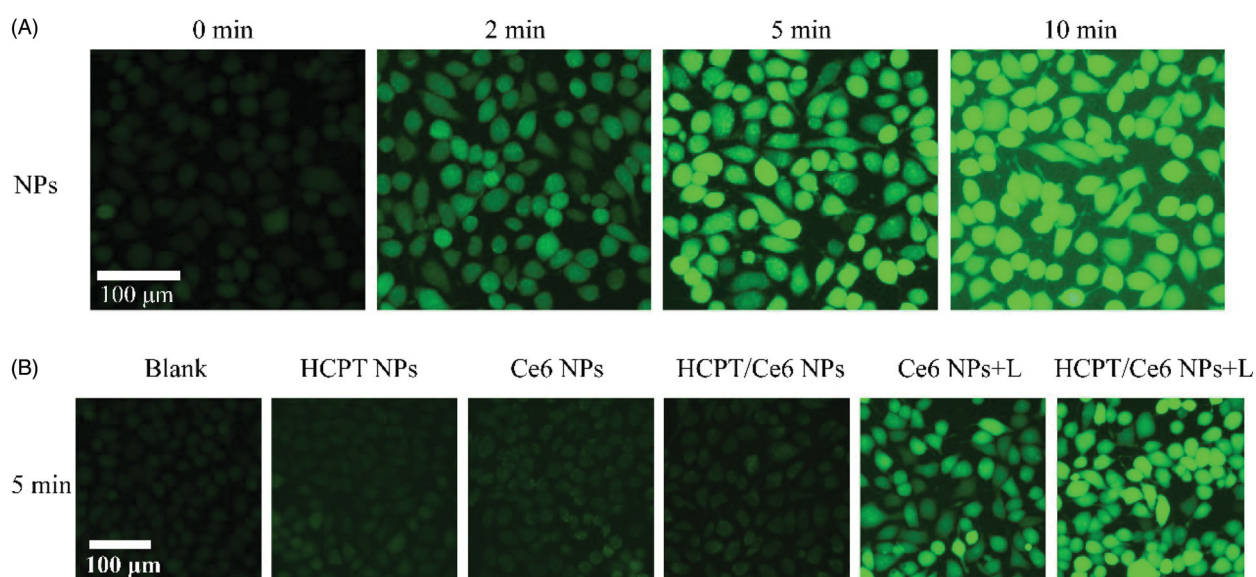


Figure 3. The representative fluorescent microscopy images of intracellular singlet oxygen generation by DCFH-DA in 4T1 cells incubated with HCPT/Ce6 NPs (with laser) for different laser irradiation times (A) and incubated with different formulations (B). Scar bar: 100 μm .

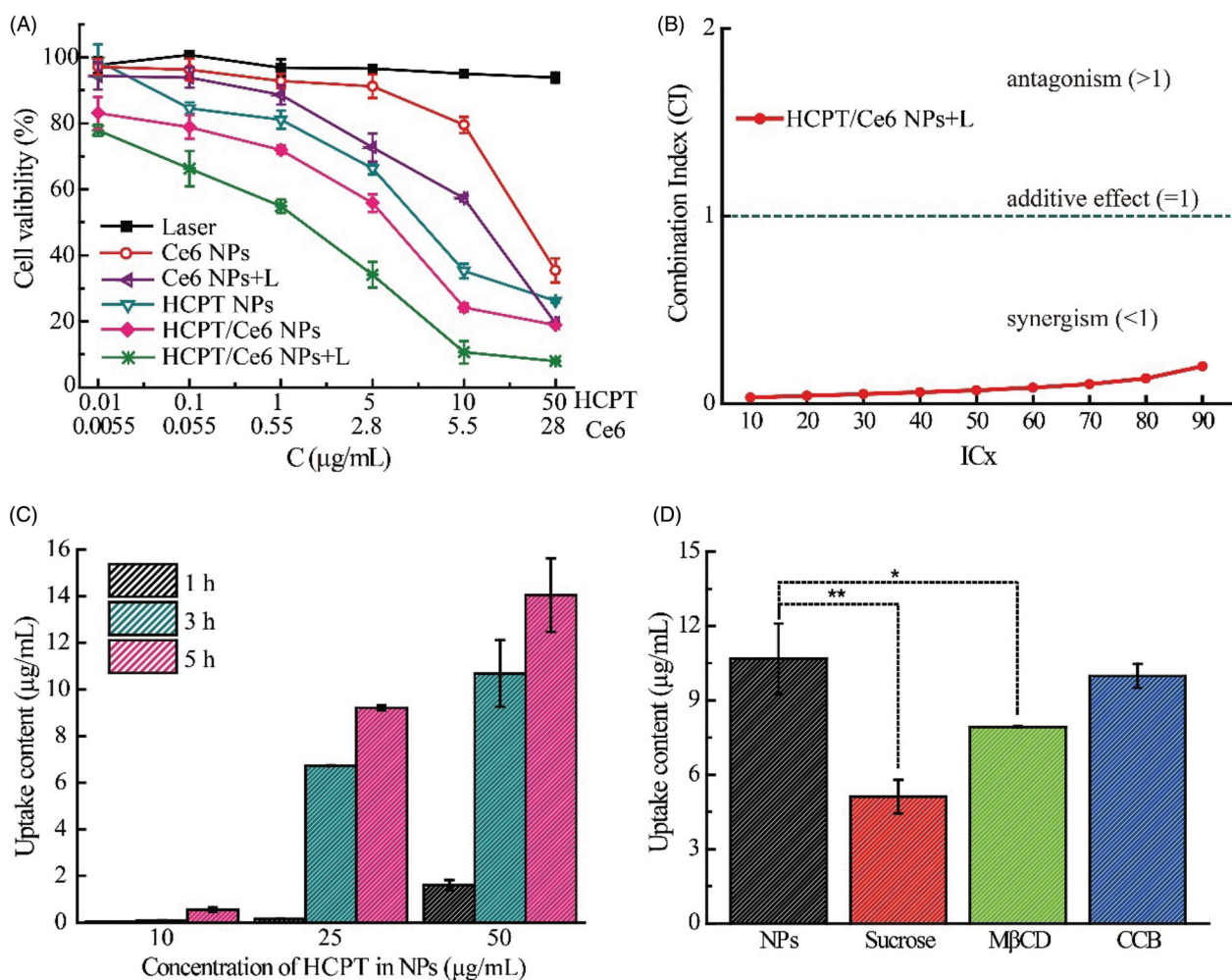


Figure 4. *In vitro* cytotoxicity of HCPT/Ce6 NPs (with laser) toward 4T1 cells after incubation for 48 h ($n=6$) (A); Combination index (CI) values of HCPT/Ce6 NPs (with laser) against 4T1 cells (B); Cellular uptake detection of HCPT/Ce6 NPs toward 4T1 cells at different HCPT concentrations and incubated times ($n=3$) (C); Cellular uptake detection of HCPT/Ce6 NPs toward 4T1 cells with different cellular uptake inhibitors ($n=3$) (D). ** $p < .001$ vs. HCPT/Ce6 NPs without cellular uptake inhibitors, * $p < .05$ vs. HCPT/Ce6 NPs without cellular uptake inhibitors.

associated to the C–H stretching vibrations and C–O stretching vibrations, respectively (Xu et al., 2019b). The typical peaks mentioned above, such as 2924, 2889, 1722, 1654, 1596, 1504, 1109 cm^{-1} could also be found in the spectrum of physical mixture of HCPT/Ce6/Chol-PEG₂₀₀₀ and HCPT/Ce6 NPs except for slight displacement and intensity decrease, which verified the successful loading of the drugs and possible molecular interactions among HCPT/Ce6/Chol-PEG₂₀₀₀ in the NPs (Huang et al., 2020). Mentionably, the characteristic band at 1723 cm^{-1} , which represented the C=O stretching vibration for the terminal lactone ring of HCPT, emerged in the FT-IR spectra of both raw HCPT and HCPT/Ce6 NPs (1722 cm^{-1}). The reservation of the band verified that HCPT remained lactone form in the NPs, which was different from clinically available HCPT injection (solubilized at pH 8.5~10.5) and guaranteed the efficiency of HCPT (Zhang et al., 2018).

3.2. In vitro release assay

The *in vitro* release profiles of HCPT/Ce6 NPs were recorded in Figure 2(D). It was clear that approximately 100% of Ce6

released at 12 h, when only 40% of HCPT released. The sustained release of HCPT continued for about 120 h, which should be attributed to the hydrophilic PEG shell formed by the amphiphilic block polymer Chol-PEG₂₀₀₀ and extended in the periphery of the NPs, that prevented its interaction with the release medium (Guo et al., 2018). However, as the macrocyclic Ce6 molecule was too large to be reserved in the core of the NPs, it released rapidly than HCPT, which would benefit for its fast elimination from the blood so as to prevent its sunlight photosensitivity after taking effect in specific tissues (Xu et al., 2019a). Besides, the distinct release profiles of HCPT and Ce6 could do favor to guarantee the PCI phenomenon-mediated combinational chemo-photodynamic therapy, that was, exerting the photodynamic effect of the preferentially released Ce6 and enhancing the sensitivity of the cancer cells to the subsequently released chemotherapeutic drug HCPT (Nishiyama et al., 2005).

3.3. Intracellular singlet oxygen ($^1\text{O}_2$) detection

The intracellular singlet oxygen ($^1\text{O}_2$) generation of HCPT/Ce6 NPs was investigated with the fluorogenic probe DCFH-DA.

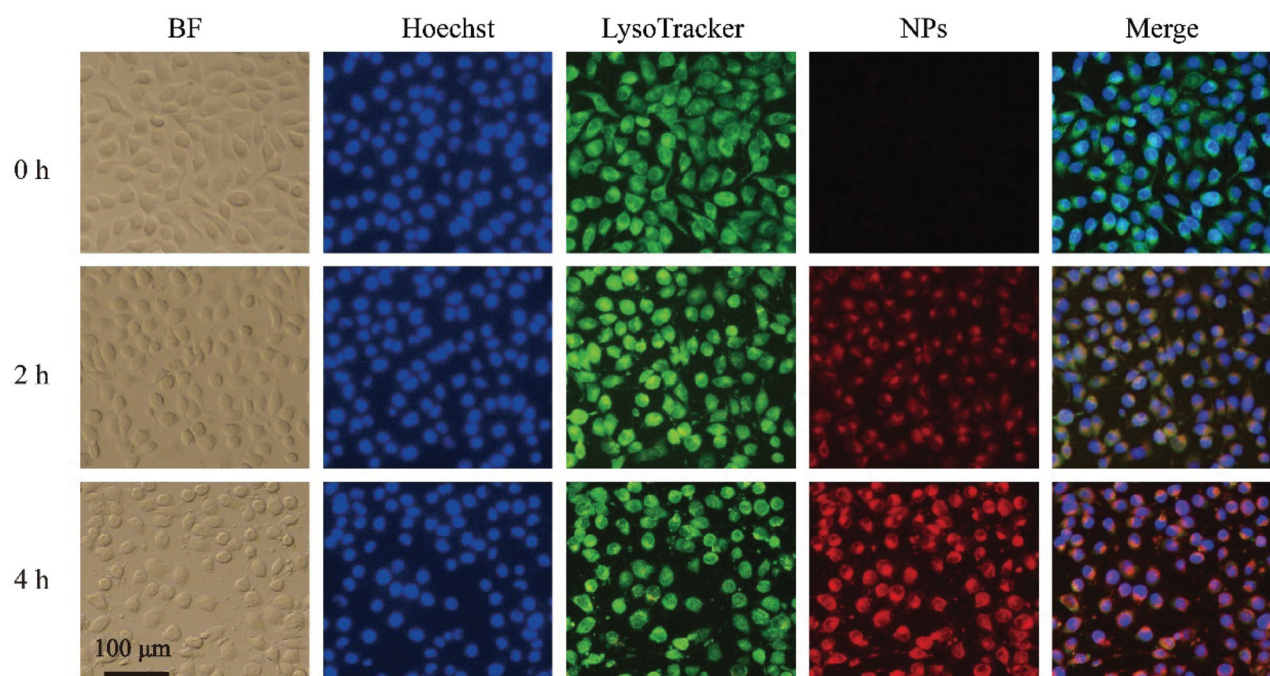


Figure 5. Representative fluorescent microscopy images of 4T1 cells incubated with HCPT/Ce6 NPs at Ce6 concentration of 5 µg/mL for different incubated times. Scar bar: 100 µm.

As shown in [Figure 3\(A\)](#), apparent green fluorescence of DCF, the product of degraded and hydrolyzed DCFH-DA in the presence of $^1\text{O}_2$ (Wang et al., 2019), was observed in 4T1 cells treated with HCPT/Ce6 NPs (with laser) and brightened against laser irradiation time, indicating the continuous $^1\text{O}_2$ production of the NPs. Besides, similarly green fluorescence of DCF was also emerged in the 4T1 cells treated with Ce6 NPs (with laser), while the 4T1 cells treated with HCPT NPs, Ce6 NPs (without laser) and HCPT/Ce6 NPs (without laser) were all absent of the DCF fluorescence ([Figure 3\(B\)](#)). The results signified that the perfect $^1\text{O}_2$ production capacity of HCPT/Ce6 NPs under laser irradiation.

3.4. In vitro cytotoxicity and cellular uptake assay

3.4.1. In vitro cytotoxicity assay

As shown in [Figure 4\(A\)](#), the cytotoxicity of all the test groups, including HCPT/Ce6 NPs (with or without laser), Ce6 NPs (with or without laser), and HCPT NPs at equivalent HCPT/Ce6 concentrations, exhibited dose-dependent proliferation inhibition profiles. There was no doubt that the cytotoxicity of HCPT/Ce6 NPs (with laser) was the most significant compared to the other groups due to combinational chemo-photodynamic effect. Besides, the 4T1 cells merely treated with laser irradiation were verified to retain their cell proliferation, indicating the nontoxicity of the laser. The IC_{50} values ([Supplementary Table S3](#)) of each group abided by the following order: HCPT/Ce6 NPs (with laser) < HCPT/Ce6 NPs (without laser) < HCPT NPs < Ce6 NPs (with laser) < Ce6 NPs (without laser) ($p < .05$). The IC_{50} value of HCPT/Ce6 NPs (with laser) was 5.6-fold lower than HCPT/Ce6 NPs (without laser), 13.7-fold lower than HCPT NPs, and 22.6-fold lower than Ce6 NPs (with laser), verified the combinational chemo-photodynamic effect of HCPT/Ce6 NPs (with

laser). HCPT NPs and Ce6 NPs (with laser) showed certain cytotoxicity due to respective chemotherapy and photodynamic therapy, which emerged slightly different (IC_{50} value of 7.80 µg/mL vs. 12.85 µg/mL). In addition, Ce6 NPs (without laser) exhibited the minimum cytotoxicity (the least IC_{50} value of 30.67 µg/mL), confirming the negligible systemic toxicity of Ce6 (without laser) (Lee et al., 2019). CI values are intensively used to evaluate the drug interaction extent in cancer therapy. Commonly, a CI value smaller than 1 signifies the synergism of the test drugs (Wang et al., 2015). In this study, the CI values of HCPT/Ce6 NPs (with laser) were figured out with the IC values of HCPT/Ce6 NPs (with laser), HCPT NPs, and Ce6 NPs (with laser), which were plotted in [Figure 4\(B\)](#). It was clear that the combined chemo-photodynamic effect of HCPT and Ce6 in HCPT/Ce6 NPs was synergistic as all the CI values were less than 1 (Luo et al., 2019).

3.4.2. In vitro cellular uptake assay

Based on the effective *in vitro* cytotoxicity of HCPT/Ce6 NPs, their cellular uptake efficiency was investigated via two method simultaneously. Firstly, the quantification of HCPT on behalf of HCPT/Ce6 NPs in 4T1 cells was performed and shown in [Figure 4\(C,D\)](#). The cellular uptake of HCPT/Ce6 NPs exhibited concentration and time-dependent profiles as the concentration of HCPT increased significantly by the raised time and concentration ([Figure 4\(C\)](#)). Besides, HCPT/Ce6 NPs showed significantly enhanced uptake efficiency than free HCPT ([Supplementary Figure S2](#)), verified the highly affinity of the 4T1 cells to HCPT/Ce6 NPs. Moreover, four endocytosis inhibitors mediating different uptake pathways were utilized to investigate the critical endocytosis pathway for the internalization process of HCPT/Ce6 NPs. As shown in [Figure 4\(D\)](#), sucrose ($p < .001$), which blocked clathrin-mediated

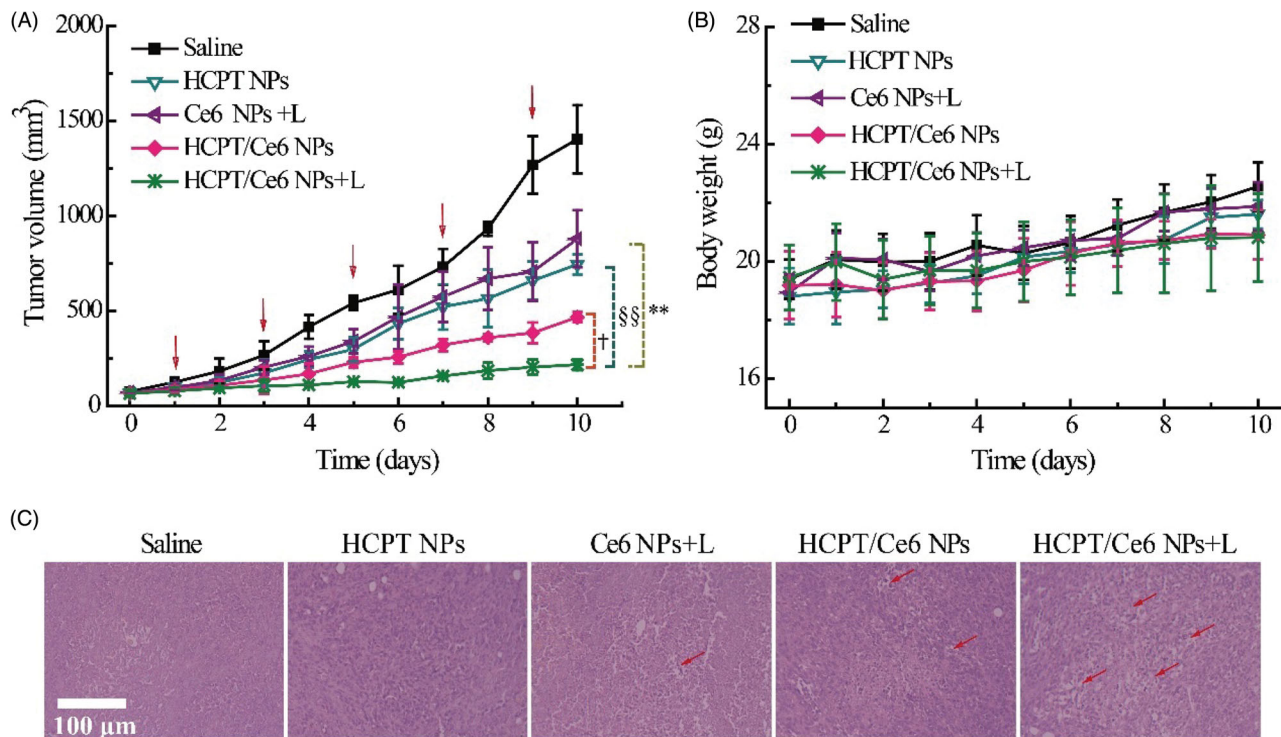


Figure 6. *In vivo* antitumor efficacy of HCPT/Ce6 NPs by the intravenous route: tumor volume changes (A), body weight changes (B), and HE staining of tumor (C) of 4T1 bearing BALB/c mice after treatment with different formulations. For each animal, five consecutive doses were given (marked by arrows). Data represent mean \pm SD ($n = 6$). $^{**}p < .001$ vs. Ce6 NPs + L (with laser) group, $^{SS}p < .001$ vs. HCPT NPs group, and $^{\dagger}p < .05$ vs. HCPT/Ce6 NPs group (without Laser).

endocytosis (Yi et al., 2015), and methyl- β -cyclodextrin (M β CD) ($p < .05$), which blocking caveolae-mediated endocytosis (Garmann et al., 2008), exhibited significantly suppression in the uptake of HCPT/Ce6 NPs, while cytochalasin B (CCB) ($p > .05$), which was the cellular uptake inhibitor of macropinocytosis-dependent endocytosis pathway (Linares et al., 2014), showed negligible restriction in the uptake of HCPT/Ce6 NPs. Obviously, the cellular uptake of HCPT/Ce6 NPs relied on clathrin-mediated endocytosis and caveolae-mediated endocytosis passway simultaneously. Secondly, the fluorescence co-localization of HCPT/Ce6 NPs was conducted with 4T1 cell lines as well. As shown in Figure 5, the legible red fluorescence of Ce6 (on behalf of HCPT/Ce6 NPs) brightened significantly against incubation time (the fourth photographs), clarified the time-dependent uptake profiles of HCPT/Ce6 NPs. Besides, the accumulation of Ce6 mainly occurred in lysosome, which verified the endocytosis process of the NPs. Moreover, it was apparent that the yellow fluorescence in the merged images, which was derived from Ce6 (red fluorescence, on behalf of HCPT/Ce6 NPs) and LysoTracker Green (green fluorescence, representing lysosome), dimmed against time (the fifth photographs). The above result should be attributed to the release of the NPs from lysosome into cytoplasm triggered by laser, which might do favor to exert the photodynamic effect of Ce6 in its effector organ (Yang et al., 2020). Besides, it was observed that the cells were gradual breakdown and the boundary between cytoplasm and nuclear lost, which signified the cytotoxicity of HCPT/Ce6 NPs as well.

3.5. *In vivo* antitumor efficacy assay

Motivated by their enhanced *in vitro* cytotoxicity, the *in vivo* antitumor efficacy assay of HCPT/Ce6 NPs (with or without laser), Ce6 NPs (with laser), and HCPT NPs were evaluated as well. As shown in Figure 6(A), the tumor growth degree of all the groups followed the order of Saline > Ce6 NPs (with laser) \approx HCPT NPs > HCPT/Ce6 NPs (without laser) > HCPT/Ce6 NPs (with laser) ($p < .001$). Obviously, the significantly suppressed tumor growth profiles of HCPT/Ce6 NPs (with laser) should be attributed to the combinational chemophotodynamic effect and efficient cellular uptake (Lv et al., 2014). Besides, the average tumor volume of HCPT/Ce6 NPs (without laser) also grown slowly during the 10 days experiment, which was even smaller than HCPT NPs ($p < .05$). The consequence could be explained by the previous report claiming that smaller particles (HCPT/Ce6 NPs: 178.9 nm vs. HCPT NPs: 252.7 nm, Supplementary Table S2) owned relatively higher population and might diffuse rapidly in tumor tissues, which resulted in their enhanced antitumor efficacy (Yue et al., 2013). In accordance with their *in vitro* cytotoxicity results, the *in vivo* antitumor consequences of HCPT NPs and Ce6 NPs (with laser) also exhibited insignificant difference with each other ($p > .05$), indicating the effectiveness of both chemotherapy and photodynamic therapy. Besides, tumor pictures of each group were shown in Supplementary Figure S3, which identified with their tumor growth profiles. Moreover, the tumor tissue section (Figure 6(C)) by hematoxylin and eosin (H&E) staining showed numerous sectional nucleus shrinkage and necrosis for HCPT/Ce6 NPs (with laser)

(marked by arrows), which indicated abundant cell disruption in the tumor (Zhao et al., 2020). However, the necrosis areas were decreased in HCPT/Ce6 NPs (without laser) and Ce6 NPs (with laser) groups, while for Saline and HCPT NPs, the phenomenon of cell disruption was totally absent. The H&E staining consequences also demonstrated the enhanced anti-tumor efficacy of HCPT/Ce6 NPs under laser irradiation.

3.6. In vivo toxicology

Body weight variation as the index of systemic toxicity was monitored everyday during the 10 days. As shown in Figure 6(B), all the treated groups showed incremental body weight progress and analogous with the control group ($p > .05$), indicating the absent of potential systemic toxicity (Yao et al., 2015). Besides, the pathological photographs of all organs (Supplementary Figure S4) for different groups were absent of inflammation and injury, verifying the excellent biocompatibility of all the test formulations as well (Chen et al., 2019b). Additionally, Supplementary Table S4 listed the biochemistry parameters of different groups, and the treated groups exhibited insignificant difference compared with the control group ($p > .05$), that was to say, all the formulations would not induce evidently hepatic or renal injury/dysfunction (Jing et al., 2020).

4. Conclusion

In this study, high payload HCPT/Ce6 NPs assembled by the collaborative interaction among HCPT/Ce6/Chol-PEG₂₀₀₀ were successfully fabricated for combinational chemo-photodynamic therapy. The obtained NPs showed excellent mono-dispersity, uniform rod-like morphology, and good storage stability in aqueous solution. HCPT/Ce6 NPs owned the ability to produce abundant intracellular ROS upon laser irradiation, possessed significantly effective *in vitro* cytotoxicity, and had enhanced cellular uptake efficiency. As a result, with specific laser irradiation, HCPT/Ce6 NPs presented remarkably stronger *in vivo* antitumor efficacy but negligibly systemic toxicity. In conclusion, HCPT/Ce6 NPs could be regarded as potential cancer treatment strategy via combined chemo-photodynamic therapy in clinic.

Acknowledgments

This work was technically supported by Shandong Collaborative Innovation Center for Antibody Drugs and Engineering Research Center for Nanomedicine and Drug Delivery Systems.

Disclosure statement

The authors declare that they have no known competing financial interests or personal relationships that could have appeared to influence the work reported in this paper.

Funding

This work was financially supported by the National Natural Science Foundation of China [no. 22073039], the Natural Science Foundation of

Shandong Province of China [no. ZR2018LB023], the Project of Shandong Province Higher Educational Science and Technology Program [no. J18KA071], the Open Project of Shandong Collaborative Innovation Center for Antibody Drugs [no. CIC-AD1831, no. CIC-AD1832], and Tai-Shan Scholar Research Fund of Shandong Province of China [no. 319190201].

References

- Bar-Zeev M, Livney YD, Assaraf YG. (2017). Targeted nanomedicine for cancer therapeutics: towards precision medicine overcoming drug resistance. *Drug Resist Updat* 31:15–30.
- Chen H, You S, Cai Q, et al. (2019a). Design and synthesis of a fluorescent amino poly(glycidyl methacrylate) for efficient gene delivery. *J Mater Chem B* 7:1875–81.
- Chen H, Zeng X, Tham HP, et al. (2019b). NIR-light-activated combination therapy with a precise ratio of photosensitizer and prodrug using a host-guest strategy. *Angew Chem* 131:7723–8.
- Feitosa VA, Almeida VCd, Malheiros B, et al. (2019). Polymeric micelles of pluronic F127 reduce hemolytic potential of amphiphilic drugs. *Colloids Surf B Biointerfaces* 180:177–85.
- Gao D, Lo PC. (2018). Polymeric micelles encapsulating pH-responsive doxorubicin prodrug and glutathione-activated zinc(II) phthalocyanine for combined chemotherapy and photodynamic therapy. *J Control Release* 282:46–61.
- Garmann D, Warnecke A, Kalayda GV, et al. (2008). Cellular accumulation and cytotoxicity of macromolecular platinum complexes in cisplatin-resistant tumor cells. *J Control Release* 131:100–6.
- Guo Y, Zhao S, Qiu H, et al. (2018). Shape of nanoparticles as a design parameter to improve docetaxel antitumor efficacy. *Bioconjug Chem* 29:1302–11.
- Guo Y, Zhao Y, Wang T, et al. (2017a). Hydroxycamptothecin nanorods prepared by fluorescently labeled oligoethylene glycols (OEG) codendrimer: antitumor efficacy *in vitro* and *in vivo*. *Bioconjug Chem* 28: 390–9.
- Guo Y, Zhao Y, Wang T, et al. (2017b). Honokiol nanoparticles stabilized by oligoethylene glycols codendrimer: *in vitro* and *in vivo* investigations. *J Mater Chem B* 5:697–706.
- Hu F, Yuan Y, Mao D, et al. (2017). Smart activatable and traceable dual-prodrug for image-guided combination photodynamic and chemotherapy. *Biomaterials* 144:53–9.
- Huang X, Chen J, Wu W, et al. (2020). Delivery of MutT homolog 1 inhibitor by functionalized graphene oxide nanoparticles for enhanced chemo-photodynamic therapy triggers cell death in osteosarcoma. *Acta Biomater* 109:229–43.
- Jing X, Zhi Z, Zhang N, et al. (2020). Multistage tumor microenvironment-responsive theranostic nanopeanuts: toward multimode imaging guided chemo-photodynamic therapy. *Chem Eng J* 385:123893.
- Kim Y, Uthaman S, Pillarisetti S, et al. (2020). Bioactivatable reactive oxygen species-sensitive nanoparticulate system for chemo-photodynamic therapy. *Acta Biomater* 108:273–84.
- Lee J, Jenjob R, Davaa E, Yang S-G. (2019). NIR-responsive ROS generating core and ROS-triggered 5'-Deoxy-5-fluorocytidine releasing shell structured water-swelling microgel for locoregional combination cancer therapy. *J Control Release* 305:120–9.
- Li H, Niu Y. (2018). Synthesis and characterization of amphiphilic block polymer poly(ethylene glycol)-poly(propylene carbonate)-poly(ethylene glycol) for drug delivery. *Mater Sci Eng C Mater Biol Appl* 89: 160–5.
- Li W, Nakayama M, Akimoto J, Okano T. (2011). Effect of block compositions of amphiphilic block copolymers on the physicochemical properties of polymeric micelles. *Polymer* 52:3783–90.
- Li X, Vinothini K, Ramesh T, et al. (2020). Combined photodynamic-chemotherapy investigation of cancer cells using carbon quantum dot-based drug carrier system. *Drug Deliv* 27:791–804.
- Linares J, Matesanz MC, Vila M, et al. (2014). Endocytic mechanisms of graphene oxide nanosheets in osteoblasts, hepatocytes and macrophages. *ACS Appl Mater Interfaces* 6:13697–706.

- Liu G, Ma J, Li Y, et al. (2017). Core-interlayer-shell Fe₃O₄@mSiO₂@lipid-PEG-methotrexate nanoparticle for multimodal imaging and multi-stage targeted chemo-photodynamic therapy. *Int J Pharm* 521:19–32.
- Liu K, Xing R, Zou Q, et al. (2016). Simple peptide-tuned self-assembly of photosensitizers towards anticancer photodynamic therapy. *Angew Chem Int Ed Engl* 55:3036–9.
- Liu Y, Liu Y, Bu W, et al. (2015). Hypoxia induced by upconversion-based photodynamic therapy: towards highly effective synergistic bioreductive therapy in tumors. *Angew Chem Int Ed Engl* 54:8105–9.
- Luo C, Sun B, Wang C, et al. (2019). Self-facilitated ROS-responsive nano-assembly of heterotypic dimer for synergistic chemo-photodynamic therapy. *J Control Release* 302:79–89.
- Lv S, Tang Z, Li M, et al. (2014). Co-delivery of doxorubicin and paclitaxel by PEG-polypeptide nanovehicle for the treatment of non-small cell lung cancer. *Biomaterials* 35:6118–29.
- Niazi M, Zakeri-Milani P, Najafi Hajivar S, et al. (2016). Nano-based strategies to overcome p-glycoprotein-mediated drug resistance. *Expert Opin Drug Metab Toxicol* 12:1021–33.
- Nishiyama N, Iriyama A, Jang W-D, et al. (2005). Light-induced gene transfer from packaged DNA enveloped in a dendrimeric photosensitizer. *Nat Mater* 4:934–41.
- Qi S-S, Sun J-H, Yu H-H, Yu S-Q. (2017). Co-delivery nanoparticles of anti-cancer drugs for improving chemotherapy efficacy. *Drug Deliv* 24: 1909–26.
- Su Y, Wang N, Liu B, et al. (2020). A phototheranostic nanoparticle for cancer therapy fabricated by BODIPY and graphene to realize photo-chemo synergistic therapy and fluorescence/photothermal imaging. *Dyes Pigments* 177:108262.
- Sun J, Jiang L, Lin Y, et al. (2017). Enhanced anticancer efficacy of paclitaxel through multistage tumor-targeting liposomes modified with RGD and KLA peptides. *Int J Nanomedicine* 12:1517–37.
- Sun Q, He F, Bi H, et al. (2019). An intelligent nanoplatform for simultaneously controlled chemo-, photothermal, and photodynamic therapies mediated by a single NIR light. *Chem. Eng. J* 362:679–91.
- Wang J, Liu L, Ying L, Chen L. (2017). Acid-responsive metallo-supramolecular micelles for synergistic chemo-photodynamic therapy. *Eur. Polym. J* 93:87–96.
- Wang S, Li J, Ye Z, et al. (2019). Self-assembly of photosensitive and chemotherapeutic drugs for combined photodynamic-chemo cancer therapy with real-time tracing property. *Colloids Surf A Physicochem Eng Asp* 574:44–51.
- Wang W, Xi M, Duan X, et al. (2015). Delivery of baicalein and paclitaxel using self-assembled nanoparticles: synergistic antitumor effect in vitro and in vivo. *Int J Nanomed* 10:3737–50.
- Wu J, Hu X, Liu R, et al. (2019). pH-responsive and self-targeting assembly from hyaluronic acid-based conjugate toward all-in-one chemo-photodynamic therapy. *J Colloid Interface Sci* 547:30–9.
- Xiao K, Li Y, Luo J, et al. (2011). The effect of surface charge on in vivo biodistribution of PEG-oligocholeic acid based micellar nanoparticles. *Biomaterials* 32:3435–46.
- Xu J, Yu S, Wang X, et al. (2019a). High affinity of chlorin e6 to immunoglobulin G for intraoperative fluorescence image-guided cancer photodynamic and checkpoint blockade therapy. *ACS Nano* 13: 10242–60.
- Xu M, Zhang K, Liu Y, et al. (2019b). Multifunctional MoS₂ nanosheets with Au NPs grown in situ for synergistic chemo-photothermal therapy. *Colloids Surf B Biointerfaces* 184:110551.
- Yan T, Cheng J, Liu Z, et al. (2018). pH-Sensitive mesoporous silica nanoparticles for chemo-photodynamic combination therapy. *Colloids Surf B Biointerfaces* 161:442–8.
- Yang X, Shi X, Zhang Y, et al. (2020). Photo-triggered self-destructive ROS-responsive nanoparticles of high paclitaxel/chlorin e6 co-loading capacity for synergetic chemo-photodynamic therapy. *J Control Release* 323:333–49.
- Yao X, Chen L, Chen X, et al. (2015). pH-responsive metallo-supramolecular nanogel for synergistic chemo-photodynamic therapy. *Acta Biomater* 25:162–71.
- Yi X, Lian X, Dong J, et al. (2015). Co-delivery of pirarubicin and paclitaxel by human serum albumin nanoparticles to enhance antitumor effect and reduce systemic toxicity in breast cancers. *Mol Pharm* 12: 4085–98.
- Yue J, Liu S, Xie Z, et al. (2013). Size-dependent biodistribution and antitumor efficacy of polymer micelle drug delivery systems. *J Mater Chem B* 1:4273–80.
- Zhang R, Xing R, Jiao T, et al. (2016). Carrier-free, chemophotodynamic dual nanodrugs via self-assembly for synergistic antitumor therapy. *ACS Appl Mater Interfaces* 8:13262–9.
- Zhang Y, Yang X, Lu Z, et al. (2018). Self-assembly behavior of amphiphilic poly(ethylene glycol)-conjugated 10-hydroxycamptothecin in water and its cytotoxicity assay. *Appl Surf Sci* 459:749–59.
- Zhao Y, Cai C, Liu M, et al. (2020). Drug-binding albumins forming stabilized nanoparticles for co-delivery of paclitaxel and resveratrol: in vitro/in vivo evaluation and binding properties investigation. *Int J Biol Macromol* 153:873–82.
- Zheng Y, Li Z, Chen H, Gao Y. (2020). Nanoparticle-based drug delivery systems for controllable photodynamic cancer therapy. *Eur J Pharm Sci* 144:105213.
- Zhou M, Zhang X, Yang Y, et al. (2013). Carrier-free functionalized multi-drug nanorods for synergistic cancer therapy. *Biomaterials* 34:8960–7.